

Modeling the 2017 September 10 solar energetic particle event using the iPATH model

Zhe-Yi Ding^{1,2}, Gang Li^{2*}, Jun-Xiang Hu² and Shuai Fu^{2,3}

¹ School of Geophysics and Information Technology, China University of Geosciences (Beijing), Beijing 100083, China;

² Department of Space Science and CSPAR, University of Alabama in Huntsville, Huntsville, AL 35899, USA; gangli.uah@gmail.com

³ Lunar and Planetary Science Laboratory, Macau University of Science and Technology, Macau 519020, China

Received 2020 February 2; accepted 2020 April 18

Abstract On 2017 September 10, a fast coronal mass ejection (CME) erupted from the active region (AR) 12673, leading to a ground level enhancement (GLE) event at Earth. Using the 2D improved Particle Acceleration and Transport in the Heliosphere (iPATH) model, we model the large solar energetic particle (SEP) event of 2017 September 10 observed at Earth, Mars and STEREO-A. Based on observational evidence, we assume that the CME-driven shock experienced a large lateral expansion shortly after the eruption, which is modeled by a double Gaussian velocity profile in this simulation. We apply the in-situ shock arrival times and the observed CME speeds at multiple spacecraft near Earth and Mars as constraints to adjust the input model parameters. The modeled time intensity profiles and fluence for energetic protons are then compared with observations. Reasonable agreements with observations at Mars and STEREO-A are found. The simulated results at Earth differ from observations of *GOES*-15. However, the simulated results at a heliocentric longitude 20° west to Earth fit reasonably well with the *GOES* observation. This can be explained if the pre-event solar wind magnetic field at Earth is not described by a nominal Parker field. Our results suggest that a large lateral expansion of the CME-driven shock and a distorted interplanetary magnetic field due to previous events can be important in understanding this GLE event.

Key words: Sun: coronal mass ejections (CMEs) — Sun: magnetic fields — Sun: particle emission

1 INTRODUCTION

Solar energetic particle (SEP) events are historically classified into two broad categories: impulsive and gradual events (Cane et al. 1986; Reames 1995, 1999). In this paradigm, impulsive SEPs are accelerated at solar flares and propagate along the interplanetary magnetic field (IMF) to Earth with a rapid rise and decay phase in the particle time intensity profiles. In comparison, gradual SEPs are accelerated via the diffusive shock acceleration mechanism at coronal mass ejection (CME)-driven shocks. Because shocks are of large scale and last much longer than flares, these events are characterized by a prolonged intensity profile and often higher fluences than impulsive events. Large gradual SEP events are of particular concern because the accompanying high-energy protons pose the most serious radiation threats to astronauts living beyond

low-Earth orbit and can damage electronics on satellites in space (Desai & Giacalone 2016). In some of the largest events, accelerated particles can reach energies up to several GeV, leading to significant increases in particle count rates through neutron monitors at the Earth’s surface and are known as ground level enhancements (GLEs). Large SEP events are usually associated with fast shocks and high ambient energetic particle intensity (referred to as seed particles) prior to the shock (Kahler 1996; Kahler et al. 2000). The increasing abundance of seed particles is possibly from preceding flares (Mason et al. 1999) or preceding CMEs (Gopalswamy et al. 2004; Li & Zank 2005). Li et al. (2012) proposed a “twin-CME” scenario for GLE events in which two CMEs erupt from the same or near active region (AR) within a period of 9 hours. The preceding CME and its driven shock disturbs the coronal and interplanetary environment and leads to enhanced turbulence level which facilitates a more efficient acceleration at the

* Corresponding author

second CME-driven shock. The scenario was later extended to large SEP events (Ding et al. 2013).

The most recent GLE event occurred on 2017 September 10, classified as GLE 72 (Mishev et al. 2018). An X8.2 class solar flare erupted around 15:35 UT from AR 12673 at S09W88, followed by a wide and very fast CME. The eruption was observed well by multiple spacecraft at different longitudes, providing a stereo view of this extreme case. The halo CME was first observed by the Solar and Heliospheric Observatory (SOHO) Large Angle and Spectrometric Coronagraph (LASCO) at 16:00 UT, with a reported linear speed of $\sim 3136 \text{ km s}^{-1}$ from the CDAW catalog. Before this extreme eruption, there were multiple preceding eruptions between September 4 and September 9 and the eruption directions varied from the longitude of 4° to 105° (Luhmann et al. 2018). However, this event would not be classified as a “twin-CME” (Li et al. 2012), because the closest preceding CME erupted at 23:12 UT on 2017 September 9, ~ 17 hours before the main eruption, exceeding the time interval threshold of 13 hours (Ding et al. 2014) as a twin-CME. The global extreme ultraviolet (EUV) waves (Liu et al. 2018; Hu et al. 2019), signatures of a flux rope and a long current sheet (Seaton & Darnel 2018; Warren et al. 2018; Yan et al. 2018) were recorded by the Solar Dynamics Observatory (SDO). Liu et al. (2019) studied the geometry and kinematics of the CME-driven shock. They argued that the close shock arrival times at Earth and Mars are a result of large lateral expansion of the shock early in the eruption. They suggested that a large lateral expansion of the shock can affect particle acceleration and consequently the observations at different longitudes. Large lateral expansion of the CME-driven shock for large CME eruptions has been investigated previously. Gopalswamy et al. (2012) examined the white-light CME evolution and noted a rapid and large lateral expansion of the CME that erupted on 2010 June 13. Kwon et al. (2015) noted the apparent width of halo CMEs as seen from multiple spacecraft was related to the expanding shock with a 360° envelope. Recent works (e.g. Liu et al. 2017, 2019; Zhu et al. 2018) have suggested that lateral expansions of a shock occur frequently in large eruptions. However, the effects of lateral expansion on SEPs have not been considered before. In this work, we will examine this problem.

Energetic particles associated with this fast CME were observed at Earth and Mars as well as the Solar Terrestrial Relations Observatory A (STEREO-A). GLE was recorded by several neutron monitoring stations at about 16:15 UT on 2017 September 10 (Mishev et al. 2018; Guo et al. 2018). The different energy channels from the instruments onboard Geostationary Operational Environmental Satellite 15 (GOES-15) indicate an in-

tensive and long-lasting enhancement of energetic particle intensity (Guo et al. 2018; Bruno et al. 2019). This event, observed at Earth, has a soft spectrum at high energies compared with most GLE events in solar cycle 23 (Gopalswamy et al. 2018; Cohen & Mewaldt 2018; Bruno et al. 2019). On September 10 at around 19:50 UT, the high energy protons were detected by the Radiation Assessment Detector (RAD) (Hassler et al. 2012) from Mars Science Laboratory (MSL) (Zeitlin et al. 2018; Ehresmann et al. 2018; Lee et al. 2018; Guo et al. 2018). Later, highly energetic protons were observed with a slow increase at STEREO-A at around 08:00 UT on 2017 September 11 (Guo et al. 2018; Lee et al. 2018).

Attempts at modeling particle acceleration and transport of SEP events have been undertaken by many groups (e.g. Heras et al. 1995; Kallenrode 1997; Luhmann et al. 2007, 2010, 2017). These models treat CME-driven shock as a source of energetic particles without an acceleration process. A dynamic onion-shell model of the strong shock propagation and particle acceleration was developed by Zank et al. (2000). This model was improved by Rice et al. (2003) for shocks with arbitrary intensities, and by Li et al. (2003) to model the transport of energetic particles following a Monte Carlo approach. Li et al. (2005) further extended the model to include heavy ions. A comprehensive numerical model, developed by these authors, is called the Particle Acceleration and Transport in the Heliosphere (PATH) model. Modeling specific SEP events using the PATH model shows their reasonable agreement (Verkhoglyadova et al. 2010, 2009). Recently, Hu et al. (2017) extended PATH to a two-dimensional (2D) model, named improved Particle Acceleration and Transport in the Heliosphere (iPATH). The new model has the capability to study the characteristics of particle acceleration and transport at a 2D shock in multiple locations of the ecliptic plane. Hu et al. (2018) modeled an example gradual SEP event as observed at multiple locations.

In the iPATH model, the shock speed profile at the inner boundary is assumed to have a Gaussian form in longitude and the propagation direction of the shock is assumed to be radial. Such an assumption is for simplicity. As we discussed earlier, large lateral expansion of shocks can be common for large events. A lateral expansion implies that the opening angle of the shock will increase over time. This means that the treatment of the inner boundary of the shock profile in the iPATH model needs to be improved. In this work, we modify the inner boundary of the shock profile to examine the effect of the large lateral expansion on producing SEPs. We note that because the background solar wind is unlikely to be homogeneous, the lateral expansion and the shock profiles do not need to be homogeneous.

Therefore, there is no need to assume a symmetric eruption.

In this paper, we discuss our modeling of the 2017 September 10 GLE event employing the iPATH model. In Section 2, we describe the iPATH model and the model setup. In Section 3, we discuss the CME-driven shock configuration and shock parameters. Modeled time intensity profile are compared with *GOES-15* observation results in different energy channels. We integrate the data of proton flux from the Advanced Composition Explorer (ACE) and *GOES-15* and fit the spectrum using the Band function. The modeled spectrum is compared with observationally fitted results. We also compare the modeled time intensity profiles with the observation results at Mars and STEREO-A. We then discuss our results and conclude in Section 4.

2 MODEL

The iPATH model is a 2D MHD code plus a particle transport code developed by Hu et al. (2017). It is a continuation of the earlier one-dimensional PATH model (Zank et al. 2000; Li et al. 2003, 2005), addressing SEP events in the ecliptic plane. It contains two separate modules: the first module models the background solar wind and follows particle acceleration at the shock front, while the second module models the transport of SEPs that escaped from upstream of the CME-driven shock. Here we limit ourselves to the modifications that we introduce to the iPATH in modeling the 2017 September 10 event.

We model the propagation of background solar wind and CME-driven shock limited only in the ecliptic plane employing a 2D MHD code. For simplicity, the background solar wind is assumed to be homogeneous. We consider the 8-hour averaged in-situ solar wind observation near Earth before the CME eruption as the solar wind inputs. The CME-driven shock is treated by perturbing the inner boundary (proton number density n , solar wind speed V_{sw} and temperature T) at 0.05 AU for a short period of time (e.g. 1 hour). Such a simplified treatment is similar to the WSA-ENLIL+Cone model for space weather prediction. The inner boundary is set at 0.05 AU ($\sim 10 R_s$) in this work, thus we cannot model particle acceleration in the low corona. Modeling CME eruption in the low corona needs a more detailed description about the magnetic field and the corona condition. However, a CME-driven shock can be formed in the low corona (Gopalswamy et al. 2013; Liu et al. 2009) and some of the highest energy particles are produced within several solar radii. Modeling this part of SEPs is beyond the scope of the iPATH model. In this work, we introduce two Gaussian velocity profiles to account for both a lateral expansion of the shock and any inhomogeneity in the background solar wind. Specifically,

we consider the following eruption profile

$$A(\phi) = \begin{cases} A_1 e^{-\frac{(\phi-\phi_{c_1})^2}{2\sigma_1^2}} \\ (0 < t < D_1) \\ A_2 e^{-\frac{(\phi-\phi_{c_2})^2}{2\sigma_2^2}} H[\phi - \phi_{\min}] * H[\phi_{\max} - \phi] \\ (0 < t - t_s < D_2) \end{cases} \quad (1)$$

where A_1 and A_2 are the perturbed model parameters (number density, speed, temperature) at longitudes ϕ_{c_1} and ϕ_{c_2} . The angles ϕ_{c_1} and ϕ_{c_2} are the central longitude of the two Gaussian distributions. The variances σ_1 and σ_2 are related to the full width at half maximum (FWHM) of the perturbed width. For the second profile, we identify a range given by $[\phi_{\min}, \phi_{\max}]$ as the perturbed range associated with the lateral expansion. D_1 and D_2 are the perturbing duration of two eruption profiles, and t_s is the start time of the second eruption, which we take as the start time of the lateral expansion. H is the Heaviside function. For simplicity, the background IMF is assumed to be a Parker spiral,

$$B_r = B_0 \left(\frac{R_0}{r} \right)^2; B_\phi = B_r \left(\frac{\Omega r \sin \theta}{u_{\text{sw}}} \right) (r \gg R_0), \quad (2)$$

where B_r and B_ϕ are the radial and azimuthal components of the IMF at heliocentric distance r respectively. u_{sw} is solar wind speed. $\theta = 90^\circ$ corresponds to the magnetic field in the ecliptic plane. B_0 is the radial component of the IMF at R_0 .

After perturbing the inner boundary, the CME-driven shock is followed in the code and the shock parameters are calculated at every time step. From these shock parameters we obtain the dynamic timescale $t_{\text{dyn}} = \frac{R}{dR/dt}$. Balancing t_{dyn} with the acceleration timescale yields the maximum particle momentum p_{max} (Drury 1983)

$$t_{\text{dyn}} = \int_{p_0}^{p_{\text{max}}} \frac{3s}{s-1} \frac{\kappa}{U_{\text{shk}}^2} \frac{1}{p} dp, \quad (3)$$

where p_0 is the injection momentum, s is the shock compression ratio, κ is the diffusion coefficient of particle and U_{shk} is the shock speed in the upstream frame. Once p_{max} is obtained, the particle distribution function in the outermost parcel (j_r, k_ϕ) at each time step t_k is given by,

$$f(j, k, p, t_k) = c_1 * \epsilon_{j,k} n_{t_k, k} p^{-\beta} H[p - p_{\text{inj}}^{j, k}] * H[p_{\text{max}}^{j, k} - p] \exp\left(-\frac{E}{E_0}\right) \quad (4)$$

where $\beta = \frac{3s_{j,k}}{s_{j,k}-1}$, $\epsilon_{j,k}$ is the injection efficiency and $n_{t_k, k}$ is the upstream solar wind density at the time t_k in front of the parcel (j_r, k_ϕ) . p_{inj} is the particle injection momentum. E is the particle energy and E_0 is the kinetic energy corresponding to the maximum particle momentum p_{max}

obtained in Equation (3). In the above, H is the Heaviside function. c_1 is a normalization constant,

$$c_1 = 1 / \int_{p_{\text{inj}}^{j,k}}^{p_{\text{max}}^{j,k}} p^{-\beta} \left\{ H[p - p_{\text{inj}}^{j,k}] * H[p_{\text{max}}^{j,k} - p] \right\} d^3 p. \quad (5)$$

Note that this functional form is different from previous works (e.g. Li et al. 2005; Hu et al. 2017), where the exponential tail $\exp(-E/E_0)$ was not included. In Drury (1983), the dynamical time t_{dyn} in Equation (3) is to be understood as the average time for accelerating particles from p_{inj} to p_{max} . Clearly, some portion of these particles would take a longer time than t_{dyn} . However, when $t > t_{\text{dyn}}$, shock parameters cannot be regarded as constant anymore, so we expect a roll-over of $f(p)$ near p_{max} . This, of course, is the consequence of a finite acceleration time. In an earlier paper, Forman & Drury (1983) examined the effect of finite time analytically and demonstrated that the particle distribution function at higher momentum manifests exponential decay of the diffusion coefficient, which is a function of particle momentum. Ellison & Ramaty (1984) adopted an exponential decay tail at high energy $\sim \exp(-E/E_0)$ to account for the effect of finite shock size and finite acceleration time. Some recent numerical simulations by Zuo et al. (2011) and Kong et al. (2019) which examined particle acceleration at a prescribed shock showed that the time dependent particle spectra are consistent with a power law with an exponential tail. With these considerations, we adopt Equation (4).

To model SEP events at multiple locations simultaneously, the iPATH model relies on a 2D onion shell module to keep track of energetic particles in the shock complex. At the j -th time step, the j -th shell (the outermost shell) is generated and divided longitudinally into different parcels (j_r, k_ϕ) with an angular width of 5° . Particles accelerated at the shock front experience convection with the parcel and diffusion between parcels. Note that particles only diffuse in parcels whose $p_{\text{max}}^{j,k}$ are greater than the particles' momentum p . This is because for parcels with $p_{\text{max}}^{j,k} < p$, there is no excited wave turbulence that can trap these particles. Particles can escape when they diffuse far enough ahead of the shock. Zank et al. (2000) assumed an escape length $l = 4\lambda_{\text{esc}}$, where $\lambda_{\text{esc}} = \frac{\kappa_{\text{rr}}}{U_{\text{shk}}}$ is the scatter length scale and κ_{rr} is the particle upstream diffusion coefficient in the direction of shock normal. Within the length l , the excited wave density is significantly higher than that of the ambient solar wind. If the wave intensity has no x -dependence, then the particle distribution function decays exponentially with the escape length in the shock front. This allows one to obtain the escaped particle distribution function. Alternatively, Li et al. (2005) calculated the number of escaped particles explicitly instead of using the particle distribution function. Note, the escape boundary

is related to each individual parcel. In this work, we follow Li et al. (2005) and obtain the escaped particle number with momentum p at time t_k and at longitude ϕ related to the outermost parcel (j_r, k_ϕ) by,

$$N_{\text{esc}}(k, p, t_k) = \sum_{j=1}^{J(k,p)} \frac{1}{2\sqrt{\pi}} \frac{\Delta R^* N_{j,k}(t_k - 1)}{r_{j,k}^*} \left\{ \exp(-x^2) + \frac{\sqrt{\pi} r_{j,k}^*}{\Delta R^*} [1 - \text{erf}(x)] \right\}, \quad (6)$$

where $N_{\text{esc}}(k, p, t_k)$ is the number of particles that escaped from the shock complex at time t_k and longitude ϕ within $d^3 p$ phase space; $J(k, p)$ is the shell number for which $p_{\text{max}} = p$; $(\Delta R^*)^2 = 4\kappa_{j,k} * (t_k - t_{k-1}) + 2([r_{j+1,k}(t_k) - r_{j,k}(t_k)]/2)^2$ decides how many particles escape from the parcel (j, k) . This parameter is larger for high energy particles since the diffusion coefficient κ increases with momentum. $N_{j,k}(t_k - 1)$ is the particle number in the parcel (j, k) before diffusion, $r_j^* = (r_{j,k} + r_{j+1,k})/2$ represents the heliocentric distance of the center of parcel (j, k) , $x = (r_{\text{esc}} - r_j^*)/\Delta R^*$ is a dimensionless parameter and $r_{\text{esc}} = r_{J(k,p),k} + l$ represents the escaping boundary for particles with momentum p .

Once particles escape from the shock complex, they propagate along the IMF in the relatively undisturbed solar wind. We closely follow Hu et al. (2017) in describing the transport of escaping particles in the second module of the iPATH model. In particular, we also include the cross-field diffusion and apply the backward stochastic differential equation method. The cross-field diffusion is governed by a term $\sim \nabla \cdot (\kappa_\perp \cdot \nabla f)$ (see eq. (18) of Hu et al. (2017)), where κ_\perp is the perpendicular diffusion coefficient of energetic particles. Hu et al. (2017) calculated κ_\perp from the parallel diffusion coefficient κ_\parallel based on Non-Linear Guiding Center (NLGC) theory. In the NLGC theory, the solar wind turbulence is assumed to have a geometry of a “slab+2D”, where the slab component describes Alfvénic fluctuation along the background field and the 2D turbulence describes how the background field line (here the Parker field) meanders. An important parameter describing the 2D component of the turbulence is the bend-over scale l_{2D} (Shalchi et al. 2010). In the work of Hu et al. (2017), the radial dependence of l_{slab} and l_{2D} was ignored. Hu et al. (2018) considered a more general case of,

$$l_{\text{slab}} \sim r^\alpha; l_{2D} \sim r^\alpha, \quad (7)$$

where α is a parameter and close to 1. In this work, we set $\alpha = 0.8$ and assume the square of the turbulent magnetic field $\delta B^2 \sim r^{-3}$, thus the radial dependence of κ_\parallel and κ_\perp utilized in Hu et al. (2018) has the following form

$$\kappa_\parallel \sim v^{\frac{4}{3}} B^{\frac{5}{3}} r^{\frac{2}{3}\alpha+3}; \kappa_\perp \sim v^{\frac{10}{9}} B^{-\frac{7}{9}} r^{\frac{8}{9}\alpha-1} \quad (8)$$

where v is particle speed, B is the background magnetic field and r the heliocentric distance. In this work, we set $\kappa_{\perp}/\kappa_{\parallel}$ to be 0.0099 at 1 AU for a 1 MeV proton. With this choice of κ_{\perp} , we examine cross field transport of energetic particles and discuss the observations at Mars and STEREO-A, which, as we show below, depend strongly on κ_{\perp} .

3 RESULTS

For our simulation, we average 8 hours of solar wind observation before the CME eruption as a guide to the background solar wind inputs. This yields a solar wind speed of 500 km s^{-1} , a magnetic field of 3.9 nT and a number density of 0.8 cm^{-3} at 1 AU. Note that there were some preceding CMEs, which mostly affected the number density of these three parameters. To account for the recovery of the corona after the preceding CME, we consider the 8-hour averaged number density of 3.5 cm^{-3} before shock arrival. As expressed in Equation (1), we use a double Gaussian profile for the velocity disturbance and the corresponding parameters describing these two Gaussian profiles are listed in Table 1. To model the large lateral expansion, we utilize a large variance for the second Gaussian distribution but limit the perturbation only within the longitudes of $[\phi_{\min}, \phi_{\max}] = [10, 90]$. The durations of the perturbations (D_1, D_2) are both set to be 1 hour and the start time (t_s) for the second perturbation is at 1 hour. The injection efficiency is assumed to be 1% for $\theta_{\text{BN}} = 0$ (i.e. parallel shock geometry). We set the ambient turbulence level $\delta B^2/B^2$ to be 0.5 at 1 AU.

Figure 1 displays the locations of various spacecraft when the event occurred and plots the scaled number density for two cases: one for the single Gaussian perturbation and the other for a double Gaussian perturbation. When the CME erupted, Earth was located at $r = 1.0 \text{ AU}$ with $\phi = 0^\circ$ and Mars was located at 1.66 AU and $\phi = 157.5^\circ$; STEREO-A is located at 0.96 AU and $\phi = 232^\circ$. Venus and Mercury are on the propagation path of this CME. However, there were no available data at these two locations. The CME-driven shock arrived at Earth and Mars at $\sim 50.5 \text{ h}$ and $\sim 59 \text{ h}$, respectively, after the eruption (Guo et al. 2018). Previous work by Guo et al. (2018) on this event has obtained a speed of 2600 km s^{-1} at $17.6 R_s$ with the central axis at 110° . In another study by Luhmann et al. (2018) employing the Cone model, the authors obtained a radial speed of 2500 km s^{-1} at $21.5 R_s$ with the center axis at 108° . In our simulation with a single Gaussian profile, shown in Figure 1 (a), we assumed the central axis is along $\phi_c = 100^\circ$ and the variance σ of the Gaussian disturbance was set to be 42° . At the inner boundary located at 0.05 AU ($\sim 10 R_s$) we increase the solar wind speed to 2400 km s^{-1} and the number densi-

ty from the background by a factor of 4 at ϕ_c , and the disturbance lasts 1 hour. With these parameters, our simulated shock arrival time is 49.2 h at Earth and 58.5 h at $\phi = 155^\circ$ near Mars, in reasonable agreement with observations. However, with these parameters, the eastern flank of the shock, magnetically connecting to Earth, is very weak and it does not accelerate particles to high energies. As noted by Liu et al. (2019), large lateral expansion of CME-driven shock could lead to enhanced SEPs for observers that are connected to the shock flank. To evaluate the effect of the large lateral expansion, panel (b) of Figure 1 depicts the shock profile applying a double-Gaussian profile with parameters given in Table 1. As we can see, a high density blob now appears in the eastern flank, leading to a locally enhanced shock compression ratio. The modeled shock arrival times are also similar to observations: 48.5 h at Earth and 58.1 h at the longitude of 155° near Mars. The shock speed at Earth is about 570 km s^{-1} (Liu et al. 2019), and the modeled shock speed at Earth is about 650 km s^{-1} .

Figure 2 plots the evolution of shock parameters in the ecliptic plane. Three observers at 1 AU with different longitudes: $0^\circ, 10^\circ, 20^\circ$ are chosen. The white dashed lines in the figure are IMF lines assuming a solar wind speed of 500 km s^{-1} . From panel (a) we can see that the eastern flank of the shock maintains a quasi-parallel geometry for the entire propagation, implying that the eastern flank of the shock has a higher efficiency to accelerate particles. Panel (b) shows the evolution of the shock speed. We note that the shock speed is smaller than 1200 km s^{-1} most of the time when Earth is connected to the shock fronts. Panel (c) depicts the maximum particle energy at shock fronts as the shock propagates from $10 R_s$ to 1 AU. The maximum energy occurs near the Sun at a longitude $\sim 110^\circ$. However, even along the field line connecting to Earth, the maximum energy can reach hundreds MeV early on. This is due to large lateral expansion: the presence of the second Gaussian profile leads to a larger compression ratio and a larger shock speed in the eastern flank. Panel (d) displays the compression ratio along the shock front during the shock propagation. There are two high-compression-ratio lobes, corresponding to the two velocity profiles. The high compression ratio in the eastern flank enhances the acceleration efficiency, indicating the importance of the large lateral expansion.

In Figure 3, the modeled time intensity profiles, plotted in panels (b) to (d), at longitudes of 0° and 20° are compared with observations by the Energetic Proton, Electron, and Alpha Detector (EPEAD-A) instrument onboard GOES-15, shown in panel (a). Note that the EPEAD-A detector has a westward-viewing angle. From our model, we choose energy channels that are similar to the observa-

Table 1 The Initial CME Parameters of Double Gaussian Distributions

Gaussian distribution	Initial speed	Density amplitude	Perturbation center	Variances
i	(km s^{-1})		ϕ_{c_i}	σ_i
1	2200	4	115°	44°
2	1400	3.4	90°	120°

Density amplitude refers to the ratio of the enhanced number density to that of the background at the inner boundary.

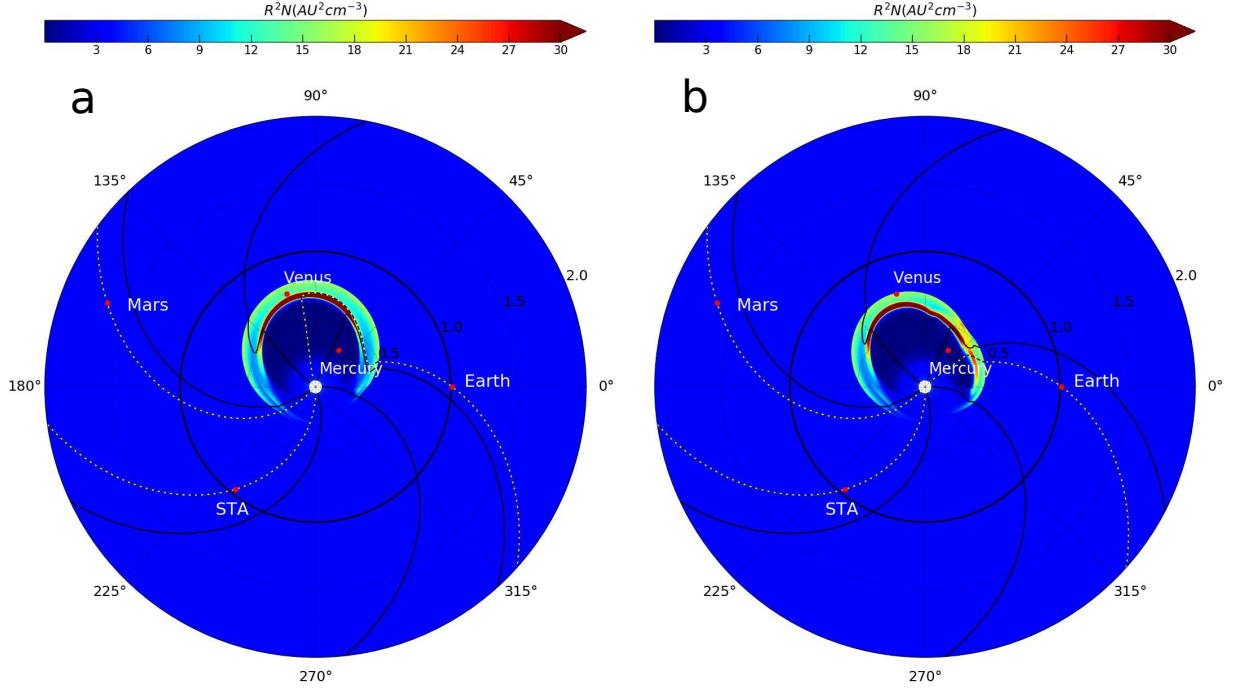


Fig. 1 Snapshots of the CME-driven shock configuration. The color scheme is for the normalized density nr^2 . The simulation domain is from 0.05 to 2 AU. The bold black circle is $r = 1$ AU. Planets Mercury, Venus, Earth and Mars and the spacecraft STEREO-A are marked as red dots, with the corresponding dashed lines the field lines passing through them. The left panel displays a symmetric eruption with a single Gaussian velocity profile and the right panel depicts the lateral expansion of CME-driven shock with two-Gaussian profiles.

tions. Because the shock arrival time differs for different longitudes, the x -axis is normalized by T_n , the shock arrival time for each observer. From panel (a) we can see that the observed intensity at all energy channels manifests substantial enhancements at the beginning of the event and are followed by slow decays. Panel (b) presents the simulated result at Earth (i.e. $\phi = 0$). The intensity undergoes a rapid enhancement at the beginning, similar to the observation. However, the decay is also very rapid, which differs considerably from the observation. As apparent in panels (b) and (d) of Figure 2, this is due to the fact that after ~ 0.5 AU, Earth is connected to a portion of the shock that has a weaker compression ratio and a low speed. Note that this connection is under the assumption that the IMF is given by a Parker field. There were some preceding CMEs in this event and the magnetic connection can therefore be different from the Parker field. We will discuss this later.

Panel (c) is the simulated result at longitude of 20° . It is interesting to note that simulation results at longitudes 20° exhibit similar decay behavior as the observation. This observer maintains relatively long duration connecting to regions of the shock that have high compression ratios. The presence of this long-duration high compression ratio is the result of the second Gaussian profile. Clearly, the assumption of the large lateral expansion of CME-driven shock is crucial for our results. We also note that if the preceding CMEs perturb the IMF such that Earth is also magnetically connected to the second Gaussian for an extended period, then we would expect observers at Earth could see results similar to panel (c). Panel (d) shows the simulated result at Earth with five times as large as κ_\perp . The results between panel (b) and panel (d) are only slightly different, which illustrate that invoking a large perpendicular diffusion alone cannot explain the Earth observation. One may think that

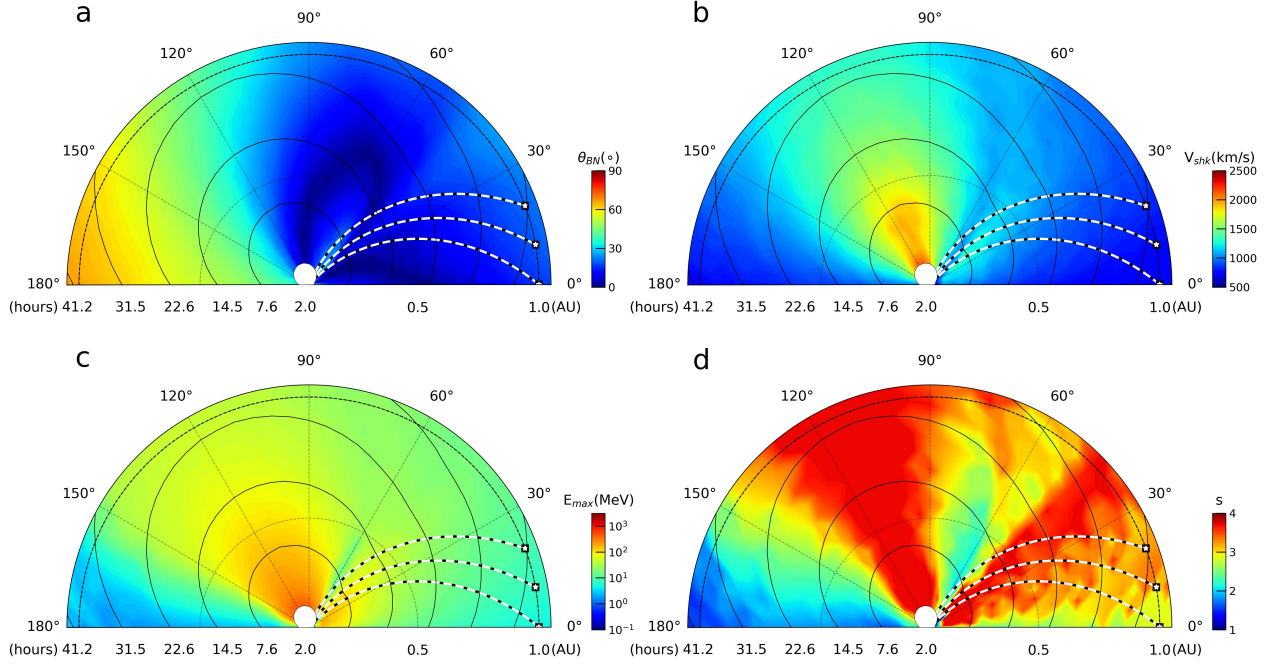


Fig. 2 The time evolution of the shock parameters along the shock front. The black solid curves indicate shock fronts at different times (labeled on the left part of the x -axis). The white dashed lines signify unperturbed Parker magnetic field lines connecting observers at longitudes of 0° , 10° and 20° . Earth is located at $\phi = 0^\circ$. The color scheme for panel (a) is the shock obliquity angle θ_{BN} (the angle between shock normal and the upstream magnetic field); for panel (b) the shock speed; for panel (c) the maximum particle energy in the shock front; and for panel (d) the shock compression ratio.

by aligning the center axis of the second Gaussian profile closer to the Earth direction can improve the simulation results at $\phi = 0^\circ$ with an ambient field that is Parker like. However, the profile of the second Gaussian profile is constrained by the shock arrival time at Earth. If one further tunes the center axis of the second Gaussian profile toward $\phi = 0^\circ$, the shock arrival time will be earlier than the observation. As a consequence, one has to decrease the amplitude of the second Gaussian, which will lead to a weaker shock and does not accelerate particles to high enough energy early on. Furthermore, if the second Gaussian profile is further towards Earth, the overall CME and shock profile will be quite distorted and appear more like two separate eruptions, which is not supported by observations.

Besides the time intensity profiles for the six energies, we also consider the event-integrated spectra at $\phi = 20^\circ$. Reasonable agreement with the observation is also obtained. The left panel of Figure 4 plots the simulated and observed event-integrated proton fluence. For the observation, we use the lower-energy data from the Low Energy Magnetic Spectrometer-120 (LEMS-120) of the Electron, Proton and Alpha Monitor (EPAM) onboard ACE, for four energy channels ranging from 330 keV to 4.75 MeV; and the high-energy data from EPEAD-A (P2-P6) and the High

Energy Proton and Alpha Detector (HEPAD, P8-P10) onboard *GOES-15*. The integration period is from 16:05 UT on 2017 September 10 to 18:30 UT on 2017 September 12.

We fit both the observed and the modeled spectra with a Band-function form (Band et al. 1993), given by,

$$\begin{aligned}
 J(E) &= CE^{-\gamma_a} \exp\left(-\frac{E}{E_0}\right) \quad \text{for } E \leq (\gamma_b - \gamma_a)E_0; \\
 J(E) &= CE^{-\gamma_a} [(\gamma_b - \gamma_a)E_0]^{\gamma_b - \gamma_a} \exp(\gamma_a - \gamma_b) \\
 &\quad \text{for } E \geq (\gamma_b - \gamma_a)E_0,
 \end{aligned} \tag{9}$$

where $J(E)$ is the particle fluence and C is a normalization constant. γ_a and γ_b are the spectral indices in the low energy region and high energy region respectively. E_0 is the spectral break energy, which typically occurs at energies of tens of MeV. Following Bruno et al. (2019), we utilize the calibration schemes by Sandberg et al. (2014) and Bruno (2017), below and above 80 MeV, respectively, to obtain the mean energy values of every channel. Using different satellite instruments, calibration schemes and integrated periods lead to different fitted parameters, Cohen & Mewaldt (2018) obtained $\gamma_a \sim 0.73$, $\gamma_b \sim 3.39$ and $E_0 \sim 19.1$ MeV. The smaller γ_a is caused by utilizing data from the Ultra-Low Energy Isotope Spectrometer

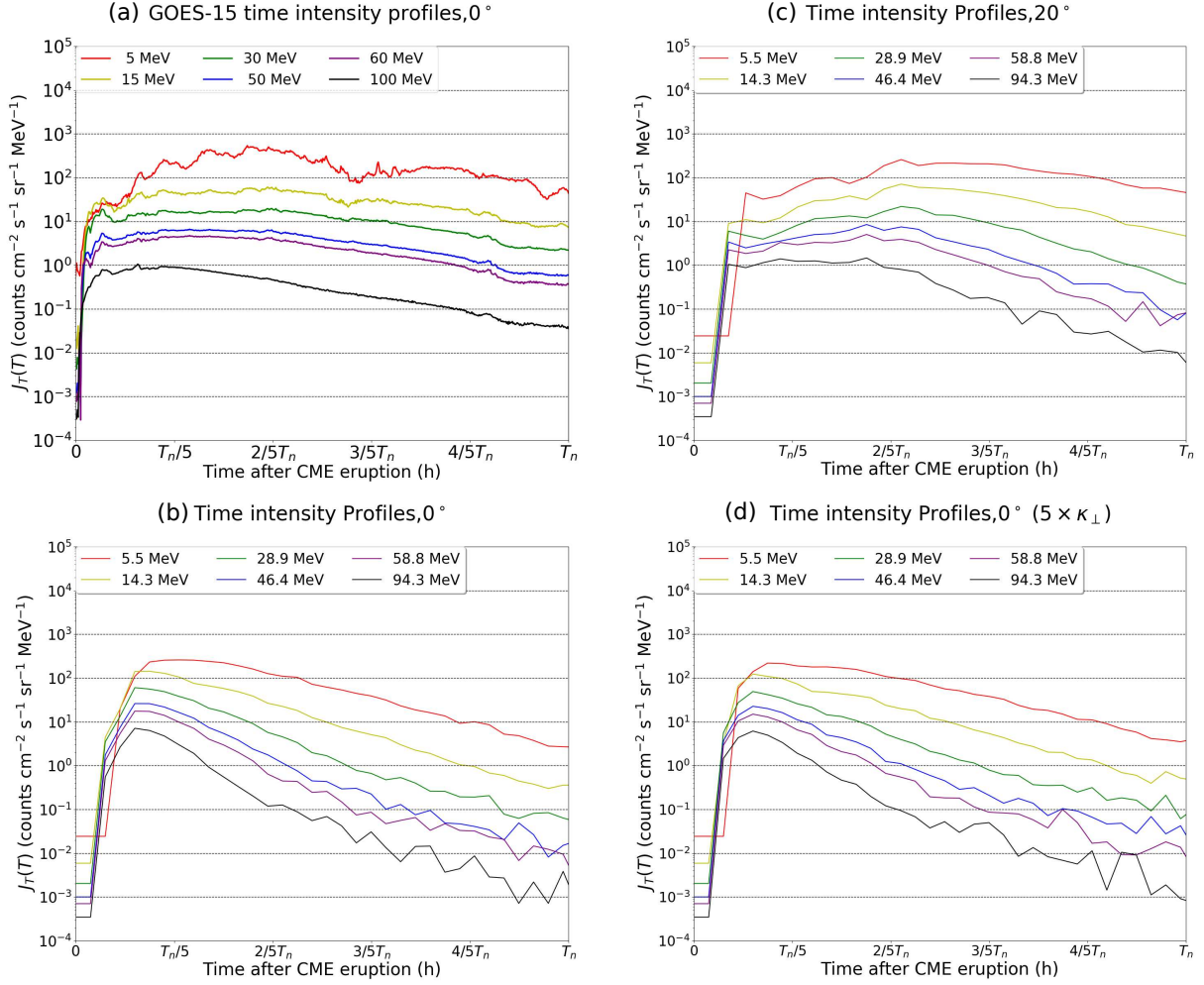


Fig. 3 Panel (a) displays the proton time intensity profile measured by *GOES-15* from onset to shock arrival. Other panels showcase the simulation results before shock arrival at different longitudes (0° , 20°). The curves with different colors correspond to different particle energies. The x -axis of all panels is the time since the eruption, normalized to T_n , where T_n is the shock arrival time for different observers.

(ULEIS) instrument onboard ACE. Bruno et al. (2019) obtained $\gamma_a \sim 1.21$, $\gamma_b \sim 4.04$ and $E_0 \sim 37.0$ MeV for a longer period, from 16:05 UT on 2017 September 10 to 00:00 UT on 2017 September 17. The fitted parameters for our period in this work are $\gamma_a \sim 1.21$, $\gamma_b \sim 3.79$ and $E_0 \sim 38.68$ MeV, similar to Bruno et al. (2019). In comparison, the fitted parameters of the modeled fluence observed at longitude of 20° are: $\gamma_a \sim 1.14$, $\gamma_b \sim 3.48$ and $E_0 \sim 50.77$ MeV. These are similar to the observations. The right panel of Figure 4 displays the simulated event-integrated proton fluence at different longitudes of 0° , 10° and 20° . Note that while the time intensity profiles at these three locations are quite different as demonstrated in Figure 3, the differences in the event-integrated spectra for these three observers are, however, small. Nonetheless, comparing the three spectral indices γ_b in the right panel confirms that the high energy portion of the spectra becomes softer as the longitude decreases. This is because

at lower longitudes the observer connects to parts of the shock flank with a compression ratio that decreases quicker.

This GLE event is one of the only two GLE events identified in solar cycle 24. The high energy spectral index of this GLE event was softer than many GLE events observed in cycle 23 (Cohen & Mewaldt 2018; Gopalswamy et al. 2018). Gopalswamy et al. (2018) suggested that the soft spectrum may be caused by poor latitudinal and longitudinal connectivities. Because the *iPATH* model is a 2D code and is limited to the ecliptic plane, we cannot consider the latitudinal effects. As to the longitudinal connection, our results suggest that the observation at Earth (with $\phi = 0^\circ$) is very close to the simulation results at longitude of 20° . Note that our simulation assumes the background magnetic field is described by a Parker field. Distortion of the background field is possible due to preceding CMEs. There were multiple CMEs

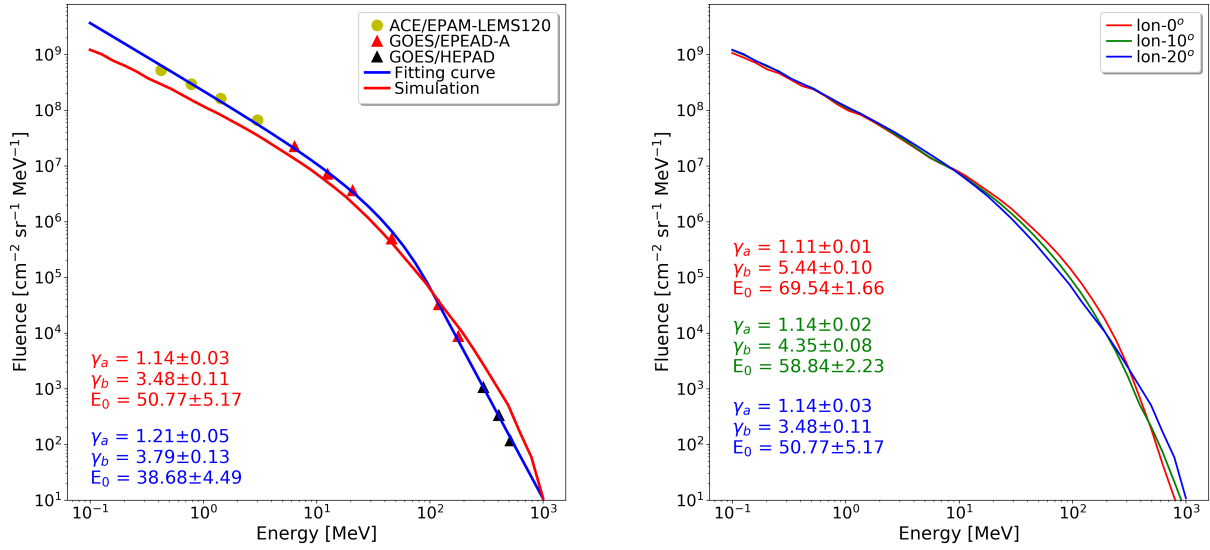


Fig. 4 Time interval-integrated proton fluence. *Left panel*: The yellow solid dots represent the fluences from the instrument EPAM-LEMS120 onboard ACE. The red solid triangles and black solid triangles represent the fluences with the instrument EPEAD-A and HEPAD onboard GOES-15. The blue curve is the fit to the observation using the Band function. The fitting parameters are shown in blue. The red curve is the modeled fluence at longitude of 20° with the red parameters from the band function fitting. *Right panel*: The modeled fluences at three different longitudes (0° , 10° , 20°) and the fitting parameters are labeled with corresponding colors.

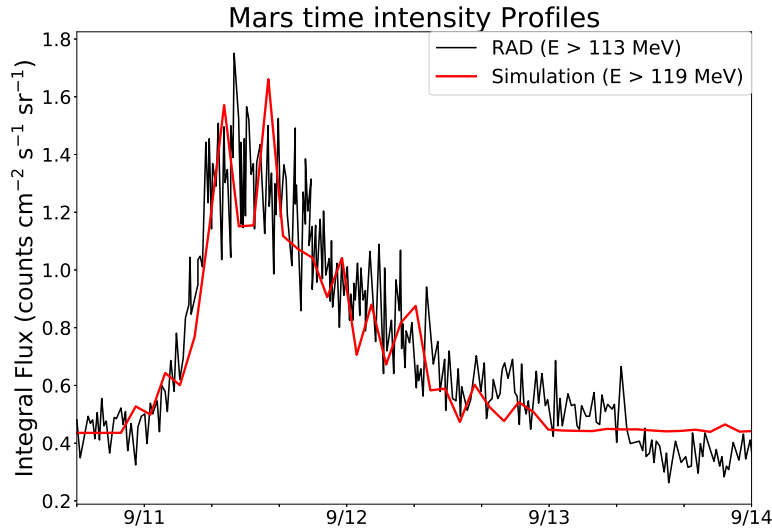


Fig. 5 The proton time intensity profiles from the observation and simulation at Mars. The black curve signifies the integral flux in the energy bands >113 MeV of the instrument RAD on MSL (adapted from Zeitlin et al. 2018). The red curve corresponds to the modeled result in the energy bands >119 MeV.

prior to the September 10 event. A large and fast CME occurred on the 6th, whose propagation direction is 40° west of Earth. At Earth, the magnetic cloud (MC) behind the shock was observed on the 8th and ended at the beginning of the 9th (Werner et al. 2019). It is very likely that the

MC is a manifestation of a flux rope structure whose two feet are anchored on the solar surface. If so, as this flux rope can further propagate out, it can affect the field that is connected to Earth on the 10th. Besides the CME on the 6th, there were also multiple smaller CMEs that occurred

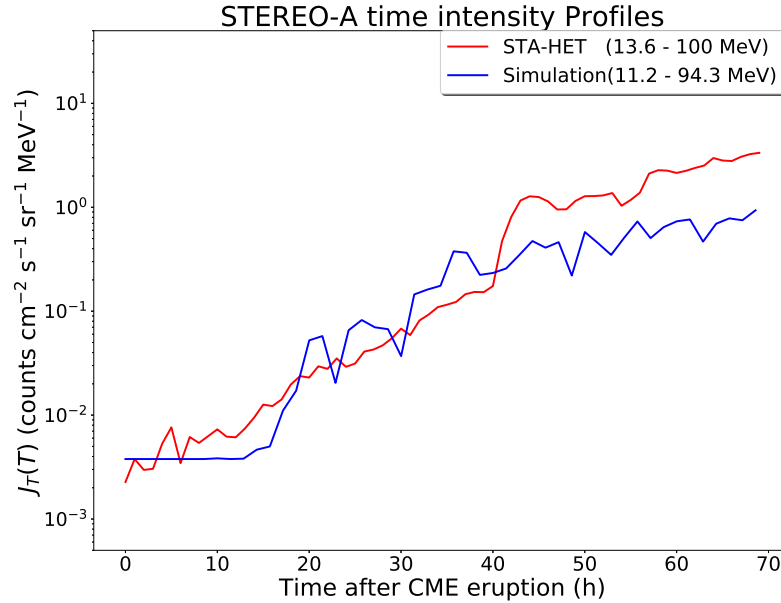


Fig. 6 The proton time intensity profiles of the observation and simulation observed by STEREO-A. The red line represents the flux in the energy bands 13.6 – 100 MeV of the instrument HET onboard STEREO-A. The blue line is the modeled result in the energy bands 11.2 – 94.3 MeV.

on the 8th and 9th. The effects of these smaller CMEs on the global magnetic field configuration are also unclear. In our simulation, we assume the background field is of Parker type, so we cannot address the connection issue. Note that the large lateral expansion of the CME-driven shock is crucial for obtaining our results. Liu et al. (2019) have suggested that the enormous lateral expansion of the shock has an important effect on SEP production for this event. However, to our knowledge, there have been no simulations addressing SEPs that consider the effect of lateral expansion of a CME and its driven shock. A large lateral expansion of the shock can affect both the time intensity profile and the even-integrated spectra. This is clearly illustrated in Figure 2, from which we can see that the observer at $\phi = 20^\circ$ can initially connect to a weak part at the edge of the first Gaussian profile (compression ratio ~ 2) of the shock, followed by a stronger part (compression ratio ~ 4) of the shock.

The high energy SEPs associated with the fast CME were also detected by Mars and STEREO-A. Zeitlin et al. (2018) reported the radiation dose rate on the surface of Mars measured by RAD, mounted on MSL’s Curiosity rover. The black curve in Figure 5 is the derived integral flux of proton energy greater than 113 MeV observed by RAD (Zeitlin et al. 2018). The proton onset time is 19:50 on 2017 September 10 at Mars, which was ~ 4 h after the CME onset. A rapid increase is detected after the onset. The red curve in Figure 5 is the simulated integral flux of

proton energy greater than 119 MeV. The event peaked on September 11, from about 4:00 to 14:00 UT (Zeitlin et al. 2018). The modeled result shows a similar peak in the figure. From panel (b) of Figure 1 we can see that Mars was initially connected to the very western flank of the shock and as the shock propagates out, the connection becomes ever weaker. Many SEPs observed at Mars are particles that undergo cross field diffusion in the IMF. They are accelerated at the stronger part of the shock. To the observer at Mars, the event is a typical eastern event. Therefore we see a clear decay phase after the peak. The shock arrival time is $\sim 02:50$ UT on 2017 September 13 followed by a clear Forbush decrease (Guo et al. 2018). The simulated shock arrival time is $\sim 02:00$ UT on 2017 September 13.

STEREO-A also observed this event. In Figure 6, the modeled proton time intensity profile in the energy bands 11.2–94.3 MeV is displayed as the blue curve. This can be compared with observations of 13.6–100 MeV protons (red curve) from the High Energy Telescope (HET) instruments onboard STEREO-A. Both of them show a gradual rising phase after the CME eruption. The absolute value of the flux is also similar. STEREO-A was at longitude of 232° which was connected to the back side of the Sun when the CME erupted. Therefore, the SEPs detected at STEREO-A must have undergone cross field diffusion as they propagated out. Our results suggest that the perpendicular diffusion

coefficients and their radial dependence used in this work are reasonable.

4 CONCLUSIONS AND DISCUSSION

In this paper, we model the 2017 September 10 SEP event applying the iPATH model. The most important assumption we made in this work is a large lateral expansion of CME-driven shock, modeled by two Gaussian velocity profiles. In previous implementations of iPATH modeling (Hu et al. 2017, 2018; Fu et al. 2019), a single symmetric Gaussian-shape velocity profile was adopted to simulate the inner boundary condition of the the CME-driven shock. To illustrate the lateral expansion, we use a velocity profile at the inner boundary consisting of two Gaussian profiles with different propagation directions and different start times. We then examine the time intensity profiles and the event-integrated spectra at multiple observation locations corresponding to observers at Earth, Mars and the STEREO-A spacecraft. We adjust the initial CME perturbation parameters such that the modeled shock arrival times at Earth and Mars are close to the observations. The introduction of a second velocity profile to mimic the lateral expansion leads to stronger particle acceleration at the eastern flank of the shock, which is necessary to understand the observation at Earth. Our model results at $\phi = 0^\circ$, which is the Earth's location, manifest similar event-integrated spectra as the ACE and GOES observations, but the modeled time intensity profile shows a clear difference from that of observation. In comparison, the model results at $\phi = 20^\circ$ are comparable to ACE and GOES observations for both the time intensity profiles and the event-integrated spectra. We interpret this by a possible field line distortion due to preceding events. There were multiple smaller CMEs before this event, which could cause the IMF to deviate from the nominal Parker configuration. We do point out that in the acceleration module of our model a Parker-like background IMF is assumed. When the unperturbed field line is non-Parker, it will affect the shock obliquity, and therefore the acceleration process. Modeling a CME with a non-Parker field is out of the scope of this work and will be pursued in a future work.

We also obtain time intensity profiles at longitudes that correspond to Mars and STEREO-A. The model results at these two locations are in good agreements with observations. Because both Mars and STEREO-A are not well connected to the CME-driven shock, SEPs observed in these locations have to undergo cross-field diffusion. The agreements between the modeling results and the observations therefore provide a confirmation of our choice of the perpendicular diffusion coefficient, and its radial dependence.

Our study suggests that modeling a realistic SEP event needs (1) an in-depth understanding of the influence of preceding CMEs, in particular the effect of a non-Parker field, and (2) taking into account possible lateral expansion. Indeed, observations have demonstrated that large lateral expansion of CME-driven shock is quite frequent in large eruptions, so considering the lateral expansion and capturing a realistic CME-driven shock profile, such as the shock speed and obliquity along the shock surface, are also crucial for any SEP modelings. We point out that lateral expansion is intrinsically inhomogeneous because the plasma conditions at different parts of the shock flank are different. In this work, we utilize a second Gaussian profile to mimic the lateral expansion. Finally, fitting observations at multiple longitudes can provide very strong constraints on the perpendicular diffusion coefficients of energetic particles. Although our simulation is for the 2017 September 10 event, it forms a nice basis for understanding other large SEP events as well.

Acknowledgements We acknowledge the use of NOAA GOES data (<https://satdat.ngdc.noaa.gov/>), the ACE data from the ACE Science Center (www.srl.caltech.edu/ACE/ASC) and the STEREO data (<https://stereo-ssc.nascom.nasa.gov/>). The work done at the University of Alabama in Huntsville is partially funded by NASA grants NNX17AI17G, 80NSSC19K0075 and 80NSSC19K0629.

References

- Band, D., Matteson, J., Ford, L., et al. 1993, ApJ, 413, 281
- Bruno, A. 2017, Space Weather, 15, 1191
- Bruno, A., Christian, E. R., de Nolfo, G. A., Richardson, I. G., & Ryan, J. M. 2019, Space Weather, 17, 419
- Cane, H. V., McGuire, R. E., & von Rosenvinge, T. T. 1986, ApJ, 301, 448
- Cohen, C. M. S., & Mewaldt, R. A. 2018, Space Weather, 16, 1616
- Desai, M., & Giacalone, J. 2016, Living Reviews in Solar Physics, 13, 3
- Ding, L.-G., Li, G., Dong, L.-H., et al. 2014, Journal of Geophysical Research (Space Physics), 119, 1463
- Ding, L., Jiang, Y., Zhao, L., & Li, G. 2013, ApJ, 763, 30
- Drury, L. O. 1983, Reports on Progress in Physics, 46, 973
- Ehresmann, B., Hassler, D. M., Zeitlin, C., et al. 2018, Geophys. Res. Lett., 45, 5305
- Ellison, D. C., & Ramaty, R. 1984, Advances in Space Research, 4, 137
- Forman, M. A., & Drury, L. O. 1983, in International Cosmic Ray Conference, 2, International Cosmic Ray Conference, 267
- Fu, S., Jiang, Y., Airapetian, V., et al. 2019, ApJL, 878, L36
- Gopalswamy, N., Nitta, N., Akiyama, S., Mäkelä, P., & Yashiro, S. 2012, ApJ, 744, 72

- Gopalswamy, N., Yashiro, S., Krucker, S., Stenborg, G., & Howard, R. A. 2004, *Journal of Geophysical Research (Space Physics)*, 109, A12105
- Gopalswamy, N., Yashiro, S., Mäkelä, P., et al. 2018, *ApJL*, 863, L39
- Gopalswamy, N., Xie, H., Mäkelä, P., et al. 2013, *Advances in Space Research*, 51, 1981
- Guo, J., Dumbović, M., Wimmer-Schweingruber, R. F., et al. 2018, *Space Weather*, 16, 1156
- Hassler, D. M., Zeitlin, C., Wimmer-Schweingruber, R. F., et al. 2012, *Space Sci. Rev.*, 170, 503
- Heras, A. M., Sanahuja, B., Lario, D., et al. 1995, *ApJ*, 445, 497
- Hu, J., Li, G., Ao, X., Zank, G. P., & Verkhoglyadova, O. 2017, *Journal of Geophysical Research (Space Physics)*, 122, 10,938
- Hu, J., Li, G., Fu, S., Zank, G., & Ao, X. 2018, *ApJL*, 854, L19
- Hu, H., Liu, Y. D., Zhu, B., et al. 2019, *ApJ*, 878, 106
- Kahler, S. W. 1996, in *American Institute of Physics Conference Series*, 374, eds. R. Ramaty, N. Mandzhavidze, & X.-M. Hua, 61
- Kahler, S. W., Reames, D. V., & Burkepile, J. T. 2000, in *Astronomical Society of the Pacific Conference Series*, 206, A Role for Ambient Energetic Particle Intensities in Shock Acceleration of Solar Energetic Particles, eds. R. Ramaty, & N. Mandzhavidze, 468
- Kallenrode, M.-B. 1997, *J. Geophys. Res.*, 102, 22347
- Kong, F. J., Qin, G., Wu, S. S., et al. 2019, *ApJ*, 877, 97
- Kwon, R.-Y., Zhang, J., & Vourlidas, A. 2015, *ApJL*, 799, L29
- Lee, C. O., Jakosky, B. M., Luhmann, J. G., et al. 2018, *Geophys. Res. Lett.*, 45, 8871
- Li, G., Moore, R., Mewaldt, R. A., Zhao, L., & Labrador, A. W. 2012, *Space Sci. Rev.*, 171, 141
- Li, G., & Zank, G. P. 2005, in *International Cosmic Ray Conference*, 1, 173
- Li, G., Zank, G. P., & Rice, W. K. M. 2003, *Journal of Geophysical Research (Space Physics)*, 108, 1082
- Li, G., Zank, G. P., & Rice, W. K. M. 2005, *Journal of Geophysical Research (Space Physics)*, 110, A06104
- Liu, W., Jin, M., Downs, C., et al. 2018, *ApJL*, 864, L24
- Liu, Y. D., Hu, H., Zhu, B., Luhmann, J. G., & Vourlidas, A. 2017, *ApJ*, 834, 158
- Liu, Y. D., Zhu, B., & Zhao, X. 2019, *ApJ*, 871, 8
- Liu, Y., Luhmann, J. G., Bale, S. D., & Lin, R. P. 2009, *ApJL*, 691, L151
- Luhmann, J. G., Ledvina, S. A., Krauss-Varban, D., Odstrcil, D., & Riley, P. 2007, *Advances in Space Research*, 40, 295
- Luhmann, J. G., Ledvina, S. A., Odstrcil, D., et al. 2010, *Advances in Space Research*, 46, 1
- Luhmann, J. G., Mays, M. L., Odstrcil, D., et al. 2017, *Space Weather*, 15, 934
- Luhmann, J. G., Mays, M. L., Li, Y., et al. 2018, *Space Weather*, 16, 557
- Mason, G. M., Mazur, J. E., & Dwyer, J. R. 1999, *ApJL*, 525, L133
- Mishev, A., Usoskin, I., Raukunen, O., et al. 2018, *Sol. Phys.*, 293, 136
- Reames, D. V. 1995, *Reviews of Geophysics*, 33, 585
- Reames, D. V. 1999, *Space Sci. Rev.*, 90, 413
- Rice, W. K. M., Zank, G. P., & Li, G. 2003, *Journal of Geophysical Research (Space Physics)*, 108, 1369
- Sandberg, I., Jiggins, P., Heynderickx, D., & Daglis, I. A. 2014, *Geophys. Res. Lett.*, 41, 4435
- Seaton, D. B., & Darnel, J. M. 2018, *ApJL*, 852, L9
- Shalchi, A., Li, G., & Zank, G. P. 2010, *Ap&SS*, 325, 99
- Verkhoglyadova, O. P., Li, G., Zank, G. P., Hu, Q., & Mewaldt, R. A. 2009, *ApJ*, 693, 894
- Verkhoglyadova, O. P., Li, G., Zank, G. P., et al. 2010, *Journal of Geophysical Research (Space Physics)*, 115, A12103
- Warren, H. P., Brooks, D. H., Ugarte-Urra, I., et al. 2018, *ApJ*, 854, 122
- Werner, A. L. E., Yordanova, E., Dimmock, A. P., & Temmer, M. 2019, *Space Weather*, 17, 357
- Yan, X. L., Yang, L. H., Xue, Z. K., et al. 2018, *ApJL*, 853, L18
- Zank, G. P., Rice, W. K. M., & Wu, C. C. 2000, *J. Geophys. Res.*, 105, 25079
- Zeitlin, C., Hassler, D. M., Guo, J., et al. 2018, *Geophys. Res. Lett.*, 45, 5845
- Zhu, B., Liu, Y. D., Kwon, R.-Y., & Wang, R. 2018, *ApJ*, 865, 138
- Zuo, P., Zhang, M., Gamayunov, K., Rassoul, H., & Luo, X. 2011, *ApJ*, 738, 168